

Three new VHS–DES quasars at $6.7 < z < 6.9$ and emission line properties at $z > 6.5$

S. L. Reed^{1,2,3★}, M. Banerji^{1,2,3}, G. D. Becker^{1,4}, P. C. Hewett^{1,2}, P. Martini^{5,6}, R. G. McMahon^{2,3}, E. Pons², M. Rauch⁷, T. M. C. Abbott⁸, S. Allam⁹, J. Annis⁹, S. Avila¹⁰, E. Bertin^{11,12}, D. Brooks¹³, E. Buckley-Geer⁹, A. Carnero Rosell^{14,15}, M. Carrasco Kind^{16,17}, J. Carretero¹⁸, F. J. Castander^{19,20}, C. E. Cunha²¹, C. B. D’Andrea²², L. N. da Costa^{15,23}, J. De Vicente¹⁴, S. Desai²⁴, H. T. Diehl⁹, P. Doel¹³, A. E. Evrard^{25,26}, B. Flaugher⁹, J. Frieman^{9,27}, J. García-Bellido²⁸, E. Gaztanaga^{19,28}, D. Gruen^{21,29,30}, J. Gschwend^{15,23}, G. Gutierrez⁹, D. L. Hollowood³¹, K. Honscheid^{5,32}, B. Hoyle^{33,34}, D. J. James³⁵, K. Kuehn³⁶, O. Lahav¹³, M. Lima^{15,37}, M. A. G. Maia^{15,23}, J. L. Marshall³⁸, R. Miquel^{18,39}, R. L. C. Ogando^{15,23}, A. A. Plazas^{1,40}, A. Roodman^{21,30}, E. Sanchez¹⁴, V. Scarpine⁹, M. Schubnell²⁶, S. Serrano^{19,20}, I. Sevilla-Noarbe¹⁴, M. Smith⁴¹, R. C. Smith⁸, F. Sobreira^{15,42}, E. Suchyta⁴³, M. E. C. Swanson¹⁷, G. Tarle²⁶, D. Thomas¹⁰, D. L. Tucker⁹ and V. Vikram⁴⁴

Affiliations are listed at the end of the paper

Accepted 2019 May 1. Received 2019 May 1; in original form 2018 December 20

ABSTRACT

We report the results from a search for $z > 6.5$ quasars using the Dark Energy Survey (DES) Year 3 data set combined with the VISTA Hemisphere Survey (VHS) and *WISE* All-Sky Survey. Our photometric selection method is shown to be highly efficient in identifying clean samples of high-redshift quasars, leading to spectroscopic confirmation of three new quasars – VDES J0244–5008 ($z = 6.724$), VDES J0020–3653 ($z = 6.834$), and VDES J0246–5219 ($z = 6.90$) – which were selected as the highest priority candidates in the survey data without any need for additional follow-up observations. We have obtained spectroscopic observations in the near-infrared for VDES J0244–5008 and VDES J0020–3653 as well as our previously identified quasar, VDES J0224–4711 at $z = 6.50$ from Reed et al. We use the near-infrared spectra to derive virial black hole masses from the full width at half-maximum of the Mg II line. These black hole masses are $\simeq 1\text{--}2 \times 10^9 M_{\odot}$. Combined with the bolometric luminosities of these quasars of $L_{\text{bol}} \simeq 1\text{--}3 \times 10^{47}$, these imply that the Eddington ratios are high, $\simeq 0.6\text{--}1.1$. We consider the C IV emission line properties of the sample and demonstrate that our high-redshift quasars do not have unusual C IV line properties when compared to carefully matched low-redshift samples. Our new DES + VHS $z > 6.5$ quasars now add to the growing census of luminous, rapidly accreting supermassive black holes seen well into the epoch of reionization.

Key words: galaxies: active – galaxies: formation – galaxies: high-redshift – dark ages, reionization, first stars – quasars: individual: VDES J0224–4711 – quasars: individual: VDES J0244–5008 – quasars: individual: VDES J0020–3653 – quasars: individual: VDES J0246–5219.

* E-mail: sr525@ast.cam.ac.uk

1 INTRODUCTION

The Epoch of Reionization (EoR) represents a transformational period in the history of the Universe when it transitioned from a predominantly neutral to a predominantly ionized state. Luminous quasars are among the best probes of this era in the Universe’s history, and high signal-to-noise ratio (S/N), high-resolution spectra of the most luminous quasars can be used to determine the neutral hydrogen fraction, for example by studying the properties of the Ly α forest and the sizes of quasar proximity zones (e.g. Fan, Carilli & Keating 2006; Bolton & Haehnelt 2007, though some recent studies have questioned the usefulness of proximity zones in determining the neutral hydrogen fraction, e.g. Eilers et al. 2017; Mazzucchelli et al. 2017). Furthermore, the identification of such luminous quasars early in the Universe’s history poses significant challenges for theories of black hole seed formation and growth (e.g. Volonteri 2010; Latif et al. 2013), requiring massive seeds as well as extended periods of Eddington-limited or super-Eddington growth to explain the population (e.g. Sijacki, Springel & Haehnelt 2009).

Around 100 luminous quasars are now known at $z \sim 6\text{--}6.5$ (e.g. Bañados et al. 2016; Jiang et al. 2016; Reed et al. 2017; Wang et al. 2017). The search for luminous quasars is now being pushed to even higher redshifts, aided by the incorporation of red-sensitive CCDs and filters in wide-field ‘optical’ surveys such as the Dark Energy Survey (DES), DECals, Pan-STARRS, and HyperSuprimeCam (HSC). These improvements in area, depth, and sensitivity enable quasars to be identified at $z > 6.5$. The challenge of identifying quasars at these highest redshifts is demonstrated clearly by the fact that for the last seven years only a single quasar was known above $z = 7$ (Mortlock et al. 2011) with the redshift record only recently broken by the $z = 7.54$ quasar identified by Bañados et al. (2018). Identifying these most distant quasars requires the combination of wide-field optical surveys (in which the quasars appear as drop-outs) with sensitive near-infrared surveys (in which the quasars are detected). Near-infrared surveys such as UKIDSS (Mortlock et al. 2011; Bañados et al. 2018), the VISTA Hemisphere Survey (VHS; Venemans et al. 2015b; Pons et al. 2019), and VIKING (Venemans et al. 2013) have therefore been crucial to pushing the redshift frontiers for quasar discovery. Many of the discoveries of $z > 6.5$ quasars have come within the last year with the new data from surveys such as DES, DECals, and HSC in combination with near-infrared data from UKIDSS, VHS, and *WISE* playing a crucial part (Matsuoka et al. 2018a, b; Bañados et al. 2018; Wang et al. 2018; Yang et al. 2018). Identifying more quasars at these highest redshifts is critical in order to constrain models of reionization as well as black hole formation and growth.

In this paper we present our search for quasars with $z > 6.5$, exploiting the wide wavelength coverage provided by combining data from DES, VHS, and the *WISE* All-Sky Survey. We also present new near-infrared spectra for three of our four $z > 6.5$ quasars. The near-infrared spectra give us access to a whole host of rest-frame UV emission lines, which trace the dynamics of the quasar broad-line region (BLR). We use these emission lines to derive more robust redshifts, estimate black hole masses as well as look for evidence for powerful disc winds affecting the BLR.

Throughout this paper we assume a flat lambda cold dark matter (Λ CDM) cosmology with $\Omega_M = 0.3$, $\Omega_\Lambda = 0.70$, and $H_0 = 70.0 \text{ km s}^{-1} \text{ Mpc}^{-1}$. All magnitudes are on the AB system, which is the native photometric system for DES. For VHS and *WISE* we have used Vega to AB conversions of $J_{AB} = J_{\text{Vega}} +$

$$0.937, K_{S,AB} = K_{S,\text{Vega}} + 1.839, W1_{AB} = W1_{\text{Vega}} + 2.699, \text{ and } W2_{AB} = W2_{\text{Vega}} + 3.339.^1$$

2 PHOTOMETRIC SELECTION

2.1 Dark Energy Survey

In Reed et al. (R17 hereafter) we presented the discovery of eight $z > 6$ quasars identified using data from the first year of DES observations (Y1). The 10σ depths for DES Y1 from R17 are $g = 24.2$, $r = 23.9$, $i = 23.3$, $z = 22.5$, and $Y = 21.2$. In this paper we use the internal DES releases (known as Y1 and Y3) corresponding to the first three years of DES observations. The DES Y3 release has been published as DES Data Release 1 (Abbott et al. 2018) and covers $\sim 5000 \text{ deg}^2$ of the sky to 10σ depths of $g = 24.3$, $r = 24.1$, $i = 23.4$, $z = 22.7$, and $Y = 21.4$ in a 1.95 arcsec diameter aperture. Thus the Y3 release probes ~ 0.2 mag deeper than the Y1 data in the z band and covers almost three times the area of DES Y1. We use the catalogues produced by the DES Collaboration throughout the paper. All DES magnitudes used in the paper are PSF magnitudes unless otherwise stated.

2.2 VISTA Hemisphere Survey

The search for quasars at the highest redshifts requires the optical data from DES to be supplemented with near-infrared photometry. In particular, observations in the near-infrared J band are important to break the degeneracy in colours between cool stars and high-redshift quasars at $6.6 < z < 6.8$. We therefore also make use of photometry in the J and K_S bands from the VISTA Hemisphere Survey (McMahon et al. 2013; Banerji et al. 2015) in this work. The VHS data used here covers ~ 68 per cent of the $\sim 5000 \text{ deg}^2$ area of the DES Y3 data release, discussed in Section 2.1. The VHS data used here is based on observations obtained between 2009 November and 2015 September inclusive (European Southern Observatory, ESO, Observing Period 84 to 95 inclusive) and corresponds to VHS Public Data Release 4 (DR4). The median 5σ J_{AB} and K_{SAB} point source magnitude limits are 21.4 and 20.3 mag, respectively. The combined DES + VHS area within which we search for high-redshift quasars is $\sim 3400 \text{ deg}^2$. In this paper we make use of the VHS catalogue magnitudes measured in a 2 arcsec diameter aperture (*apermag3*) with an appropriate aperture correction for point sources.

2.3 WISE All-Sky Survey

Longer wavelength data at 3.4 and 4.6 μm (known as the $W1$ and $W2$ bands, respectively) were used from the all-sky *Wide Infrared Survey Explorer* data set (*WISE*; Wright et al. 2010). We used the unWISE reduction of the NEOWISE-R3 images (Meisner, Lang & Schlegel 2017). These coadd images are deeper than those in the AllWISE data release with 5σ point source depths of $W1_{AB} = 20.2$ and $W2_{AB} = 19.8$. The *WISE* data overlaps with the full DES + VHS area of our search and *WISE* fluxes were measured by performing forced aperture photometry on the unWISE coadds using the locations of sources from the VHS J -band catalogues.

¹http://wise2.ipac.caltech.edu/docs/release/allwise/expsup/sec5_3e.html

Table 1. Summary of the steps in the $z > 6.5$ quasar candidate photometric selection process.

Step	Description	Number removed	Number remaining
	Number of objects in catalogue		425 880 019
1	Flag criteria $Y_{\text{PSF}} \leq 21.5$ and $\sigma_Y < 0.2$ $z_{\text{PSF}} - Y_{\text{PSF}} > 0.5$ g_{PSF} and $r_{\text{PSF}} > 23.0$ σ_g and $\sigma_r > 0.1$		
2	Match to unWISE forced photometry		821 709
3	$Y - J < 1.0$	606 347	215 362
4	$Y < 21.0$	171 369	43 993
5	$6.3 < z_{\text{predicted}} < 7.2$	41 633	2360
6	$\chi^2_{\text{Quasar}} < 25.0$ and $\chi^2_{\text{BD}} > 2.0$	2081	279

2.4 Quasar candidate selection via SED fitting

In order to select high-redshift quasar candidates, a series of loose flux limits and colour cuts was first applied to the combined photometric catalogues from DES + VHS + unWISE covering $\sim 3400 \text{ deg}^2$. These cuts are summarized in Table 1 in the order in which they are applied to the data. The loose colour cuts allow us to reject sources with unphysical colours and narrow down the number of objects on which we perform full spectral energy distribution (SED) fitting. The cuts applied are broadly similar to those in R17. In that work we demonstrated that some of the high-redshift quasars recovered by our SED-fitting selection method spanned a wider range of colours compared to previous high-redshift quasar searches – for example, VDES J2250–5015 in R17 is too red in terms of its ($Y - J$) colour to satisfy the selections in e.g. Bañados et al. (2016) and Venemans et al. (2015a). To allow the inclusion of redder quasars in our sample we relaxed the ($Y - J$) colour cut further from < 0.8 used in R17 to < 1.0 in this work. The initial colour selection box is shown in Fig. 1 along with the predicted tracks of quasars and brown dwarfs and our final sample of photometric candidates that satisfy all the selection criteria.

The loose colour cuts and flux limits result in a sample of 215 362 photometric candidates. These are further cut down to 43 993 by applying a brighter Y -band flux limit to the sample given that most optical spectrographs used for spectroscopic follow-up have relatively poor response in this wavelength range. The SED-fitting method introduced in R17 was then applied to the photometric candidates in order to estimate the probabilities of the candidate being either a quasar or a brown dwarf. In the case of the quasar model fits, best-fitting photometric redshifts and extinctions were also derived for each candidate. The quasar and brown dwarf models employed were identical to those in R17 (Maddox & Hewett 2006; Maddox et al. 2012; Skrzypek et al. 2015). An example of the results of SED fitting for one of our quasar candidates, VDES J0244–5008, can be seen in Fig. 2. As the objective of this study was to identify quasars at the highest redshifts we selected candidates with a photometric redshift of > 6.3 . This study is aimed at finding quasars with $z > 6.5$ but a slightly lower photometric redshift limit was used to allow for scatter in the photometric redshift estimate. Spectroscopic confirmation of our high-redshift quasar candidates makes use of optical spectrographs (see Section 3). We therefore also imposed an upper redshift limit of $z < 7.2$, above which the $\text{Ly}\alpha$ emission line redshifts out of the range of most optical spectrographs. The candidates within this redshift range

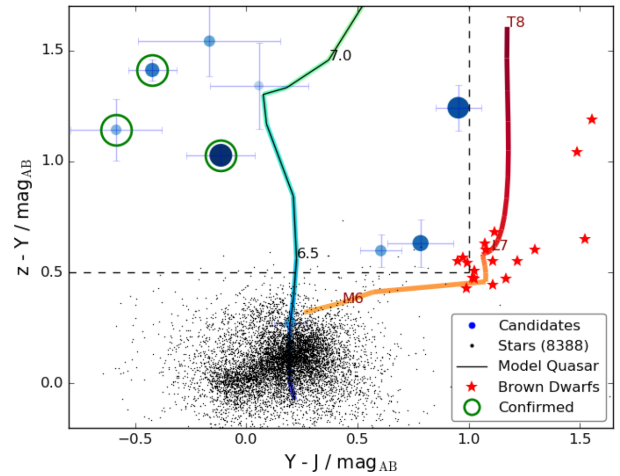


Figure 1. The initial colour selection used in this paper. The yellow–red line shows the predicted path of brown dwarfs from the models used in this paper; the red stars show the colours of known brown dwarfs taken from Kirkpatrick et al. (2011) and are mostly found outside the quasar selection box that is delineated by the dashed lines. The blue–green line shows the predicted path of quasars. The blue points show the final eight quasar candidates selected after visual inspection and the size of the points is proportional to how good their fit to a quasar model is, with the largest points having the best fit. The circled objects were spectroscopically followed up and confirmed to be quasars. The small black points are a sub-sample of the DES + VHS photometric sources shown for comparison to the location of the quasar candidates.

were then narrowed down based on their χ^2_{Quasar} and χ^2_{BD} values, which represent the reduced χ^2 values obtained from the quasar and brown dwarf model fits, respectively. Specifically, candidates with $\chi^2_{\text{Quasar}} > 25.0$ or $\chi^2_{\text{BD}} < 2$ were removed from the sample based on the distribution of values shown in Fig. 3. This led to 279 high-redshift quasar candidates. All 279 candidates were visually inspected, following which we identified eight candidates as the most probable high-redshift quasars. The colours of these eight candidates are shown in Fig. 1. During the visual inspection stage, the majority of objects removed corresponded to instances of blended sources in the unWISE coadds, which were resolved in the DES and VHS images. As the unWISE forced photometry for these blended objects was biased artificially bright, it improved their fit to a quasar model. Other sources removed include diffraction spikes, cosmic rays, and saturated objects. Of the eight remaining candidates, one (VDES J0244–5008) had already been identified by us as a high-redshift quasar candidate using DES Y1 data and was spectroscopically followed up in 2015 January (Section 3.1.3). Of the remaining seven candidates, five were detected in more than one VHS band and were therefore deemed higher priority. Two of the five candidates (VDES J0020–3653 and VDES J0246–5219) were visible during our spectroscopic observing runs (Section 3) and were therefore followed up. No spectroscopy has as yet been obtained for the other candidates. DES cut-out images for all three high-redshift quasars with spectroscopic follow-up observations can be seen in Fig. 4 and the photometry for all three sources is summarized in Table 2. For completeness we also include in Table 2 the properties of VDES J0224–4711, which is the other $z \geq 6.5$ quasar previously identified by us using DES + VHS in R17.

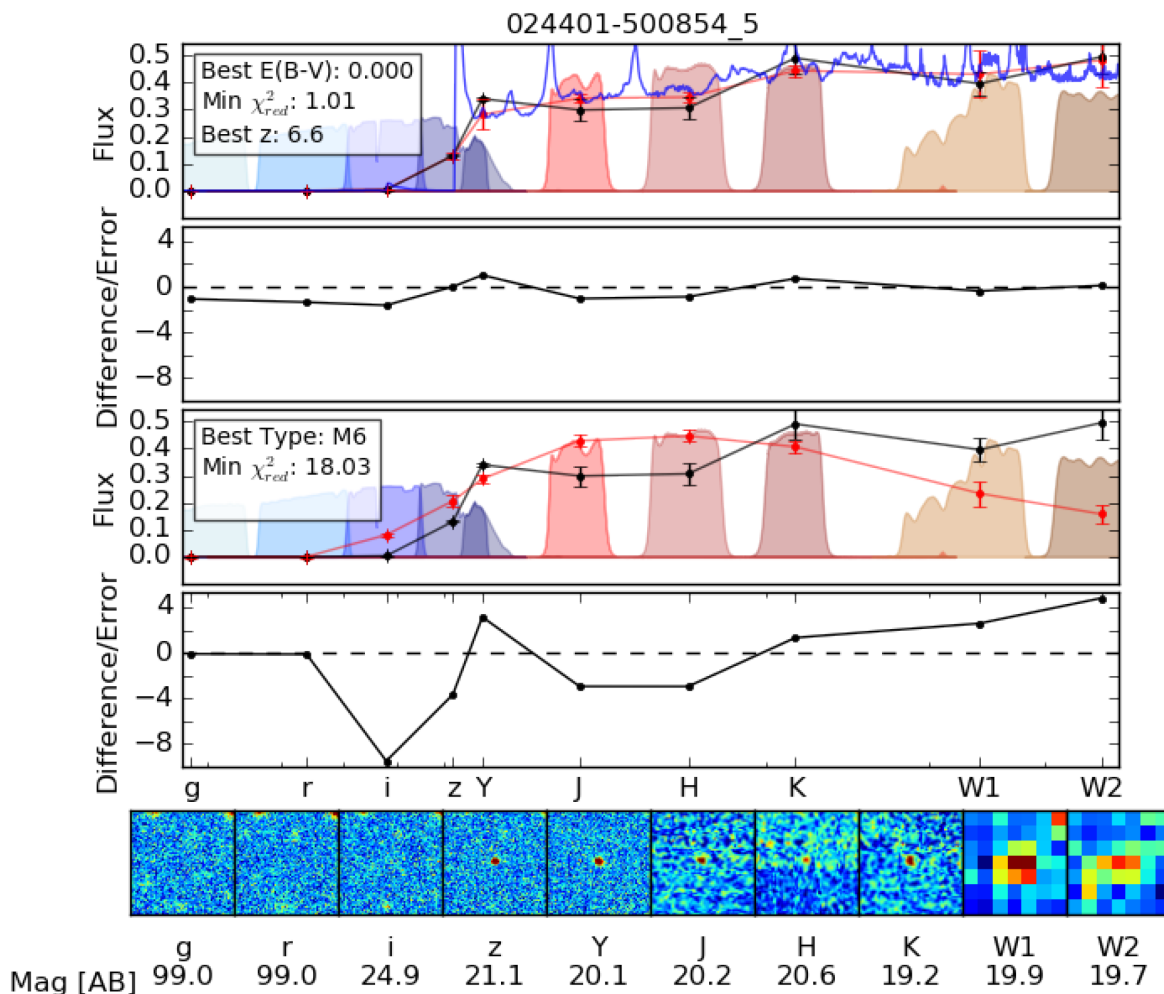


Figure 2. The SED fitting method illustrated for VDES J0244–5008, the first $z > 6.5$ candidate identified from DES data. The top two panels show the best quasar fit and the difference (between the predicted and actual values) divided by the total error (model error and actual error combined) for this fit, respectively. The next two panels show the same for the best-fitting brown dwarf model. The bottom row of images shows 20 arcsec cut-out images across the DES, VHS, and *WISE* bands. VDES J0244–5008 was confirmed as a quasar with $z = 6.724$.

3 SPECTROSCOPIC OBSERVATIONS

This section presents details of the spectroscopic observations conducted for our three $z > 6.5$ quasar candidates identified in Section 2.4. We begin by describing the optical spectroscopic observations used to confirm that our photometric candidates are true high-redshift quasars. We then present near-infrared spectra that allow us to derive emission line properties and black hole masses for these quasars. In addition to the three $z > 6.5$ quasar candidates, we also present here new optical and near-infrared spectra for the $z = 6.50$ quasar VDES J0244–4711, which was first identified in R17.

3.1 Optical spectroscopy

3.1.1 Las Campanas Clay MagE

VDES J0244–5008 was our first $z > 6.5$ quasar candidate identified using DES Y1 photometry. In 2015 January the source was observed using the Magellan Echellette (MagE) Spectrograph on the 6.5 m

Clay Telescope at Las Campanas. Details of the observational set-up can be found in Table 3. The data were reduced using a custom suite of IDL routines (e.g. Becker et al. 2012). Individual frames were flat-fielded and the sky emission subtracted using an optimal b-spline fit to the sky following Kelson (2003). Relative flux calibration was performed using standard stars. For each detector, a single one-dimensional spectrum was simultaneously extracted from all two-dimensional exposures of a given object using optimal techniques (Horne 1986). Corrections for telluric absorption were done using model transmission curves based on the ESO SKYCALC Cerro Paranal Advanced Sky Model (Noll et al. 2012; Jones et al. 2013). The MagE spectrum can be seen in the third panel of Fig. 5. The optical spectrum and the onset of the Ly α emission line (see R17 for details) imply a redshift of $z = 6.733 \pm 0.008$ for the quasar. Further to the method given in R17 the uncertainties on the redshifts were calculated by taking 100 realizations from the error spectrum and adding them to the spectrum before running them through the same redshift determination method. The uncertainty given is the σ_{MAD} from this distribution.

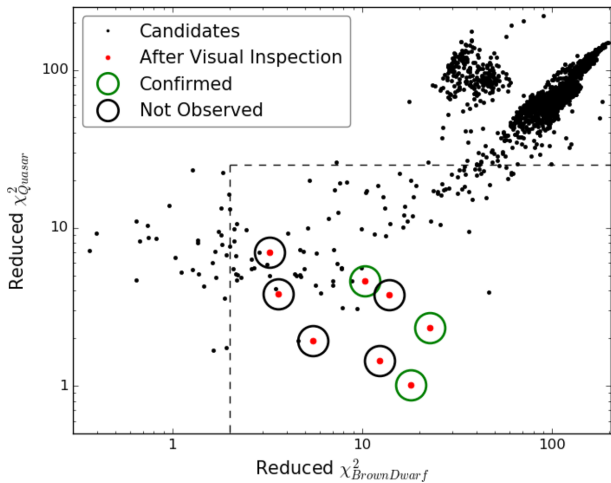


Figure 3. The results of the χ^2 SED fits for the 2360 candidates left after the predicted redshift cuts in Table 1. The dashed lines show the cuts used to narrow down the candidate list for visual inspection. These cuts remove the clearly defined locus of points that have very high χ^2 for both the quasar and brown dwarf model fits. Visual inspection showed these to primarily be objects with contamination in the Y band, such as diffraction spikes. The final eight candidates remaining after visual inspection of all sources in the selection region are shown as the red points. The spectroscopically confirmed quasars are highlighted with green circles.

3.1.2 ESO NTT EFOSC2

The two candidates – VDES J0246–5219² and VDES J0020–3653 – identified from the DES Y3 data were observed using the European Southern Observatory’s 3.6m New Technology Telescope (NTT). Observations were taken during 2016 December and 2017 November as part of programmes 098.A-0439 and 0100.A-0346, respectively. A summary of the observational set-up is given in Table 3. The spectra were reduced using a custom PYTHON library designed for reducing high-redshift quasar spectra and detailed in R17. Flat fielding and dark subtraction were done using calibration products taken during the afternoon preceding the observations. Cosmic rays were removed from the image using a PYTHON implementation (cosmics.py) of the L.A. Cosmic algorithm (van Dokkum 2001). The object was then extracted from the calibrated and cleaned image using a Gaussian extraction kernel and the response function corrected for using standard star measurements. Finally the one-dimensional spectra were flux calibrated to reproduce the observed magnitudes of the object in DES and VHS. The reduced spectra can be seen in the top two panels of Fig. 5 and confirms the identity of both candidates as high-redshift quasars. Based on the onset of the Ly α forest we derive redshifts of 6.90 ± 0.02 and 6.86 ± 0.01 for VDES J0246–5219 and VDES J0020–3653, respectively.

3.1.3 Gemini South GMOS

VDES J0224–4711 was first identified in R17 using DES Y1 data and spectroscopically confirmed as a $z = 6.50$ quasar via observations with the EFOSC2 spectrograph on the European Southern Observatory’s New Technology Telescope. Here we present a new higher spectral resolution, higher S/N rest-frame UV spectrum of

the same object taken with the GMOS spectrograph on Gemini-S. Details of the observational set-up can be found in Table 3. The data were reduced using the methods outlined in R17 for the Gemini GMOS data and are broadly similar to those employed for the NTT spectral reductions (Section 3.1.2). The new GMOS spectrum for VDES J0224–4711 can be seen in the bottom panel of Fig. 5.

The new spectrum allows for a better estimate of the quasar ionization near-zone size compared to the NTT discovery spectrum. The analysis of near-zone sizes for all our high-redshift quasars will be presented in a forthcoming paper. We also derive a new Ly α redshift of $z = 6.514 \pm 0.005$ based on this spectrum (see R17 for details on the redshift estimation method).

3.2 Infrared spectroscopy

3.2.1 Gemini South Flamingos

Near-infrared spectra were obtained for VDES J0224–4711 and VDES J0244–5008 using the Flamingos 2 (F2) spectrograph on the Gemini South telescope. We used the long-slit spectroscopy mode with a slit width of 4 pixels (corresponding to 0.72 arcsec). F2 uses a 2048x2048 Hawaii-II (HgCdTe) detector with 18 micron pixels. There are two gratings used in the set-up for these observations, the JH and HK gratings. The JH grating covers 0.9 to 1.8 micron and the HK grating covers 1.2 to 2.4 micron. These can then be combined to give coverage from 0.9 to 2.4 micron in the observed frame.

VDES J0224–4711 was observed in 2016 November and VDES J0244–5008 was observed in 2017 January. Both objects were observed for 8×200 s exposures in both JH and HK. The observations were taken in pairs using an ABBA nodding pattern. Each pair was then reduced together: One observation was subtracted from the other to remove artefacts and as a first pass at sky subtraction. The subtracted image was then flat fielded to leave a relatively clean image with a positive and negative trace visible. Each trace was extracted separately and later combined. Wavelength calibration was performed using argon lines from arc lamp spectra taken during the night of the observations. A fifth-order Chebyshev polynomial fit was used to determine the wavelength solution. After the wavelength calibration the median of the eight individual exposures was used as the final output spectrum.

The system response was calculated using observations of the AOV type standard star HIP6364, taken just preceding the observations of the target. The standard star observations were reduced in the same way as the target data with the only difference being that two pairs of observations were taken rather than four. The output spectrum of the star was then divided by an AOV spectral template³ in order to give the telluric and instrument response correction. Both the near-infrared spectra can be seen in the bottom two panels of Fig. 6.

3.2.2 VLT XShooter

VDES J0020–3653 was observed with the XShooter spectrograph on the ESO Very Large Telescope sited at Paranal Observatory in 2017 October. The observations were reduced using a custom set of IDL routines (López et al. 2016). The data reduction steps are broadly similar to those described in Section 3.1.1 We did not nod-subtract the X-Shooter near-infrared frames. Instead, a high S/N composite dark frame was subtracted from each exposure to

²This quasar was recently independently discovered by Yang et al. (2018).

³<http://axe.stsci.edu/html/templates.html>

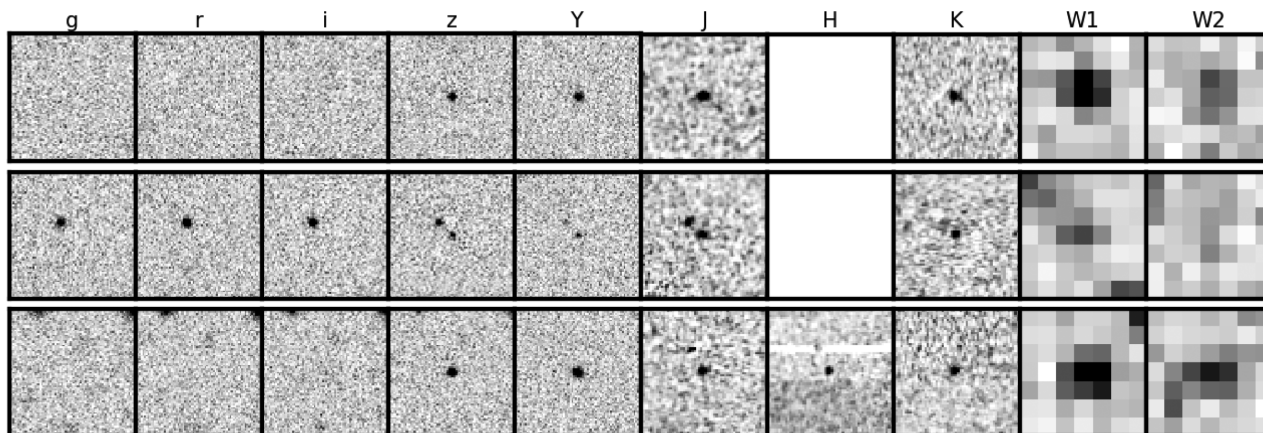


Figure 4. DES optical, VHS near-infrared, and unWISE infrared 20 arcsec cut-outs of the three new $z > 6.5$ quasars identified in this paper. Top to bottom: VDES J0020–3653, VDES J0246–5219, and VDES J0244–5008. All three quasars appear as drop-outs in the DES gri bands as expected. There is no H -band data for the top two objects. In these cut-outs north is down and east is to the left.

Table 2. Positions and magnitudes of the three new $z > 6.5$ quasars discovered in this work as well as the $z \sim 6.5$ quasar VDES J0224–4711 from R17. The g -, r -, and i -band magnitudes are given as a 5σ magnitude limits for a 2 arcsec aperture.

	VDES0224–4711	VDES J0244–5008	VDES J0020–3653	VDES J0246–5219
DES Tilename	DES0222–4706	DES0245–4957	DES0021–3706	DES0246–5205
RA (J2000)	36.11057	41.00424	5.13113	41.73289
Dec. (J2000)	$02^{\text{h}}24^{\text{m}}26^{\text{s}}.54$	$02^{\text{h}}44^{\text{m}}01^{\text{s}}.02$	$00^{\text{h}}20^{\text{m}}31^{\text{s}}.47$	$02^{\text{h}}46^{\text{m}}55^{\text{s}}.89$
	-47.19149	-50.14826	-36.89495	-52.33054
	$-47^{\circ}11'29''.4$	$-50^{\circ}08'53''.7$	$-36^{\circ}53'41''.8$	$-52^{\circ}19'49''.9$
g	> 25.0	> 24.0	> 24.0	> 24.0
r	> 25.0	> 24.4	25.53 ± 0.60	> 24.4
i	24.0 ± 0.4	> 23.9	25.01 ± 0.64	> 23.9
z	20.20 ± 0.02	21.08 ± 0.08	21.39 ± 0.04	21.85 ± 0.11
Y	19.89 ± 0.05	20.15 ± 0.05	19.98 ± 0.03	20.70 ± 0.08
J	19.75 ± 0.06	20.21 ± 0.15	20.40 ± 0.10	21.29 ± 0.19
Ks	18.99 ± 0.06	19.67 ± 0.14	19.55 ± 0.13	20.35 ± 0.21
W1	18.75 ± 0.05	19.91 ± 0.12	19.82 ± 0.14	20.09 ± 0.14
W2	18.6 ± 0.1	19.02 ± 0.15	19.71 ± 0.32	21.89 ± 0.81

Table 3. Observational details for the optical spectroscopy of the three new $z > 6.5$ quasars as well as the $z = 6.50$ quasar VDES J0224–4711 from R17.

Name	Telescope	Instrument	Exposure time (seconds)	Date	Filter	Grating/Grism
VDES J0224–4711	Gemini-S	GMOS	$300 \times 4 = 1200$	2016/10/07	RG610_G0331	R400 + _G5325
VDES J0244–5008	Clay	MagE	$600 + 1200 \times 2 = 3000$	2015/01/18	OG-590	VPH-Red
VDES J0020–3653	NTT	EFOSC2	$1800 + 1800 = 3600$	2016/12/25	OG530	Gr#16
VDES J0246–5219	NTT	EFOSC2	$2400 + 2400 = 4800$	2016/11/15	OG530	Gr#16

mitigate the effects of dark current, hot pixels, and other artefacts prior to fitting the sky. The sky model used is again described in Section 3.1.1. The final XShooter near-infrared spectrum can be seen in the top panel of Fig. 6.

4 EMISSION LINE PROPERTIES

We now consider the emission line properties derived from our near-infrared spectra in order to constrain the systemic redshifts, black hole masses, and broad-line region outflow velocities of our high-

redshift quasars. The emission lines detected in the near-infrared spectra are generally of modest S/N at the native spectral resolution of these observations. For the purposes of measuring broad emission line properties, high spectral resolution is not a prerequisite. We therefore create inverse-variance-weighted binned spectra of our quasars before spectral fitting.

Line properties are derived from the binned spectra by fitting Gaussian profiles to the broad emission lines after subtraction of a pseudo-continuum, which is made up of a power-law component to model emission from the quasar accretion disc and an Fe II template

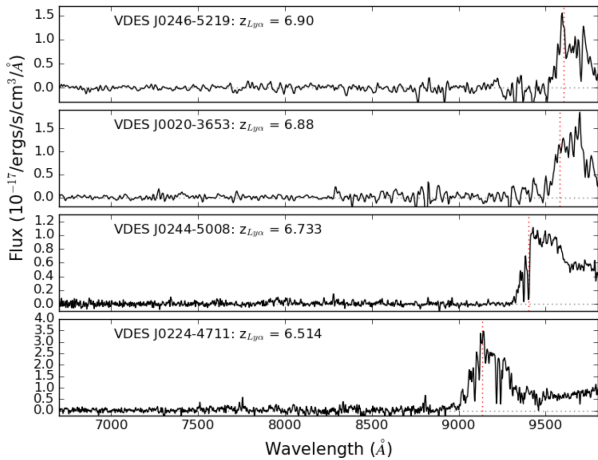


Figure 5. Optical discovery spectra of the three new $z > 6.5$ quasars identified in this work as well as the new Gemini GMOS spectrum of the $z \sim 6.5$ quasar VDES J0224–4711 (Section 3.1.1) from R17. The red dotted lines mark the derived Ly α redshift for these quasars and the redshifts derived from the onset of the Ly α emission line are indicated in the figure legend.

from Vestergaard & Wilkes (2001). Given the modest S/N in the continuum, an Fe II template results in an improved fit to the Mg II line only for the lowest redshift quasar, VDES J0224–4711. In order to model the emission line, we begin by fitting a single Gaussian to the line profile and add additional Gaussians only if they are strongly evidenced by the data and result in an improvement in the reduced χ^2 of the fit by > 10 per cent.

Uncertainties on the line properties are calculated by generating 100 realizations of the spectra with the flux at each wavelength drawn from a normal distribution with a mean value taken from the best-fitting Gaussian model and a standard deviation given by the noise spectrum. The line fitting is then run on each of these 100 synthetic spectra and the standard deviations of the resulting line-fit parameters are quoted as our formal uncertainties.

4.1 Systemic redshifts

Robust measures of quasar ionization near-zone sizes rely on an accurate estimate of the quasar systemic redshift. It is well known that redshift estimates based on the Ly α emission line can have large systematic offsets as this resonant line is affected by absorption and the kinematics therefore strongly depend on the geometry and distribution of the obscuring material, which affect the scattering of Ly α photons. Redshift estimates based on low-ionization rest-frame optical emission lines such as Mg II, 2798 Å on the other hand are generally considered more robust (Hewett & Wild 2010; Shen et al. 2016) although the Mg II line has also been known to show significant offsets of $\sim 1000 \text{ km s}^{-1}$ (Venemans et al. 2016; Mazzucchelli et al. 2017). Here we make use of our new near-infrared spectra to derive systemic redshifts based on Mg II (as the most reliable option available with our data) and compare them to the Ly α redshifts presented in Section 3.1.

The Gaussian fits to the continuum-subtracted Mg II line profiles for all three quasars can be seen in Fig. 7. While a single Gaussian provides a reasonable fit to VDES J0244–5008 and VDES J0020–3653, in the case of VDES J0224–5711 we find that two Gaussians constrained to have the same centroid are necessary in order to adequately fit the broad wings seen in the emission

line profile of this object. There is no evidence for a velocity offset between the two Gaussian components in this quasar and we therefore do not allow the centroid of the second Gaussian to be an additional free parameter in the fit.

From these Gaussian fits we infer Mg II redshifts of 6.526 ± 0.003 , 6.724 ± 0.002 , and 6.834 ± 0.004 for VDES J0224–4711, VDES J0244–5008, and VDES J0020–3653, respectively. For VDES J0244–5008, the redshift estimate is consistent with that based on the onset of Ly α but for the other two quasars, Ly α is redshifted by $\delta z \sim 0.01\text{--}0.03$ relative to Mg II.

4.2 Bolometric luminosities, black hole masses, and Eddington ratios

We calculated bolometric luminosities for our quasars from the rest-frame 3000 Å luminosities assuming a bolometric correction of 5.15 (De Rosa et al. 2011). The rest-frame 3000 Å luminosities have been calculated by fitting our quasar SED models (Section 2.4) to the available photometry for each quasar and fixing the redshift of the model to the spectroscopic redshift of the quasar estimated from the Mg II line. Both values are quoted in Table 4 and the errors are estimated by propagating the errors on the measured photometry.

Black hole masses were calculated from the full width at half-maximum (FWHM) of the Mg II line and using the calibration in Vestergaard & Osmer (2009):

$$\frac{M_{\text{BH}}}{M_{\odot}} = 10^{6.86} \left(\frac{\text{FWHM}_{\text{Mg II}}}{1000 \text{ km s}^{-1}} \right)^2 \left(\frac{L_{3000}}{10^{44} \text{ erg s}^{-1}} \right)^{0.5}. \quad (1)$$

We derived the FWHM of the Mg II from the best-fitting Gaussian model and subtracted the instrumental resolution in quadrature from this value. Uncertainties were calculated using the 100 realizations of the line profile with noise added. The FWHM of the Mg II line together with the derived black hole masses are given in Table 4. All three quasars have black hole masses of $\simeq 1\text{--}2 \times 10^9 M_{\odot}$. The typical systematic uncertainties on these black hole mass estimates are ~ 0.3 dex (Shen et al. 2019). Combining with their bolometric luminosities of $\simeq 1\text{--}3 \times 10^{47} \text{ erg s}^{-1}$ we infer Eddington ratios of close to or just above unity for all three quasars consistent with them being seen during a high-accretion growth phase. In Fig. 8 we compare the bolometric luminosities and black hole masses to other $z > 6$ quasars from the literature where such observations have been made (De Rosa et al. 2011, 2014; Mazzucchelli et al. 2017; Bañados et al. 2018). Our three new quasars have bolometric luminosities, black hole masses, and Eddington ratios that are broadly consistent with other high-redshift quasars.

4.3 C IV blueshifts

The C IV 1550 Å emission line in luminous quasars has long been known to display systematic velocity offsets of several thousand km s^{-1} blueward of systemic (Richards et al. 2002; Baskin & Laor 2005), which are widely thought to be indicative of outflowing gas in the quasar broad-line region (Konigl & Kartje 1994; Murray et al. 1995). Attention has been drawn to the large C IV blueshifts seen in the spectra of the highest redshift quasars (De Rosa et al. 2011; Mazzucchelli et al. 2017), which could indicate that strong disc winds are particularly prevalent in these systems. Changes in the C IV emission line properties of quasars – that is blueshift and equivalent width – are themselves correlated with the velocity widths and strengths of other optical and UV emission lines as well as the bolometric luminosity of the quasar (Richards et al. 2011). Recently Coatman et al. (2016) demonstrated that $z \sim 2$ quasars

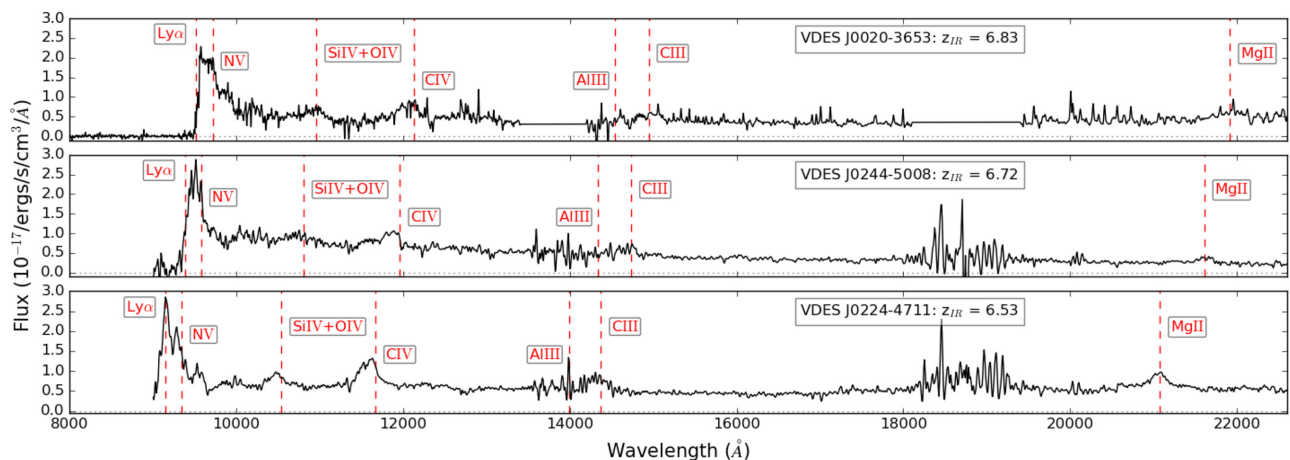


Figure 6. Near-infrared spectra of three of our four $z > 6.5$ quasars. The red lines show the positions of spectral lines in the observed frame assuming the Mg II-derived systemic redshifts from Table 4. The areas of very noisy (or blanked) flux, around 13 800 and 19 000 Å have very little flux due to the limited transmission at those wavelengths.

with high C IV blueshifts also exhibit high Eddington ratios. It is therefore interesting to explore the C IV emission line properties of our quasars in the context of these previous observations.

We fit the C IV emission lines in our three high-redshift quasars after subtracting a power-law continuum from the spectrum. Fe II emission is less strong in this region compared to the Mg II region of the spectrum and given the typical S/N of these spectra, we did not consider it necessary to include an Fe II component in the continuum. Each component of the C IV doublet is modelled as the sum of two Gaussians with a fixed velocity separation between the doublet components of 390 km s^{-1} . The use of two Gaussians to model each component of the doublet allows us to adequately reproduce the asymmetric C IV line profiles, given the typical S/N of our spectra. The C IV blueshifts are derived from the velocity centroid of the C IV emission line relative to the Mg II-derived systemic redshifts presented in Section 4.1. These blueshifts range from 1700 km s^{-1} in VDES J0020–3653 to 3200 km s^{-1} in VDES J0244–5008 (Table 4). The C IV equivalent widths are also summarized in Table 4. We also calculated C IV line properties in an analogous way for the $z = 6.82$ quasar VHSJ0411–0907 recently discovered by Pons et al. (2019), deriving a blueshift of $830 \pm 20 \text{ km s}^{-1}$ and a rest-frame equivalent width of $32 \pm 1 \text{ Å}$ for this quasar.

In Fig. 9 we compare the C IV blueshifts in our high-redshift sample with a sample of low-redshift quasars from SDSS (Shen et al. 2011), where the low-redshift C IV blueshifts have been calculated in an analogous way to the $z > 6.5$ quasars – see section 3.2 of Coatman et al. (2016). Specifically, the C IV emission line properties for the SDSS quasars were derived using systemic redshift estimates using an independent component analysis (ICA) technique from Allen & Hewett (in preparation), who do not themselves include the C IV line in the systemic redshift estimate – see Coatman et al. (2016, 2017) for a detailed discussion on this issue. The ICA redshifts are completely consistent with the Mg II redshifts for SDSS quasars, as well as for our high-redshift sample. However, using the ICA redshifts does allow us to expand the SDSS comparison sample to $z > 2.2$, where Mg II is no longer present in the SDSS spectrum. Thus, our SDSS low-redshift comparison sample is much larger than those used in previous works, for example Mazzucchelli et al. (2017). We also note that unlike some other works in the literature we make use of the C IV velocity centroid rather than the peak

velocity for all blueshift measurements. As the C IV emission line can have significant flux in the wings of the line, the centroid measure generally results in larger blueshifts compared to the peak.

As a result of these updates, a much larger fraction of the low- z SDSS quasars now display significant C IV blueshifts that are comparable to the high-redshift population. Our $z > 6.5$ quasars (as well as those studied e.g. by Mazzucchelli et al. 2017) are also among the highest luminosity, highest Eddington ratio quasars compared to the SDSS population and therefore expected to have large C IV blueshifts compared to the average SDSS quasar. If we select SDSS quasars with $\log_{10}(L_{\text{bol}}/\text{erg s}^{-1}) > 47.0$ only and compare them to the blueshifts and equivalent widths of our four $z > 6.5$ quasars we find that a two-dimensional Kolmogorov–Smirnov test is consistent with the low- and high-redshift quasar populations being drawn from the same continuous distribution. Very recently Shen et al. (2019) reached the same conclusion by comparing the C IV emission line properties of a large sample of $5.7 \lesssim z \lesssim 6.4$ quasars to lower redshift quasars from SDSS. We have deliberately not included the Mazzucchelli et al. (2017) quasars in our test as we cannot confirm that the same line-fitting prescriptions have been used to calculate C IV emission line properties for these quasars as we have done here both for the high-redshift and low-redshift SDSS quasars. At face value however there are three quasars in Mazzucchelli et al. (2017) with very large blueshifts of $> 4000 \text{ km s}^{-1}$, which would seem inconsistent with being drawn from the same distribution as the low-redshift SDSS quasars.

5 DISCUSSION AND CONCLUSIONS

We have described the discovery of three new quasars at $6.7 \lesssim z \lesssim 6.9$ identified using imaging data from the Dark Energy Survey Year 3 data release, VISTA Hemisphere Survey, and WISE. These discoveries show that our SED-fitting method to identify $z \sim 6$ quasars from wide-field imaging surveys (R17) can easily be adapted to produce clean, low-contamination samples at even higher redshifts of $z > 6.5$. The three new quasars have $J_{\text{AB}} = 20.2$ to 21.3 ($M_{1450} = -25.6$ to -26.6). They are at redshifts of 6.724, 6.834, and 6.90.

We obtained near-infrared spectra for three of the four $z \geq 6.5$ quasars identified by us using DES + VHS, to constrain their black

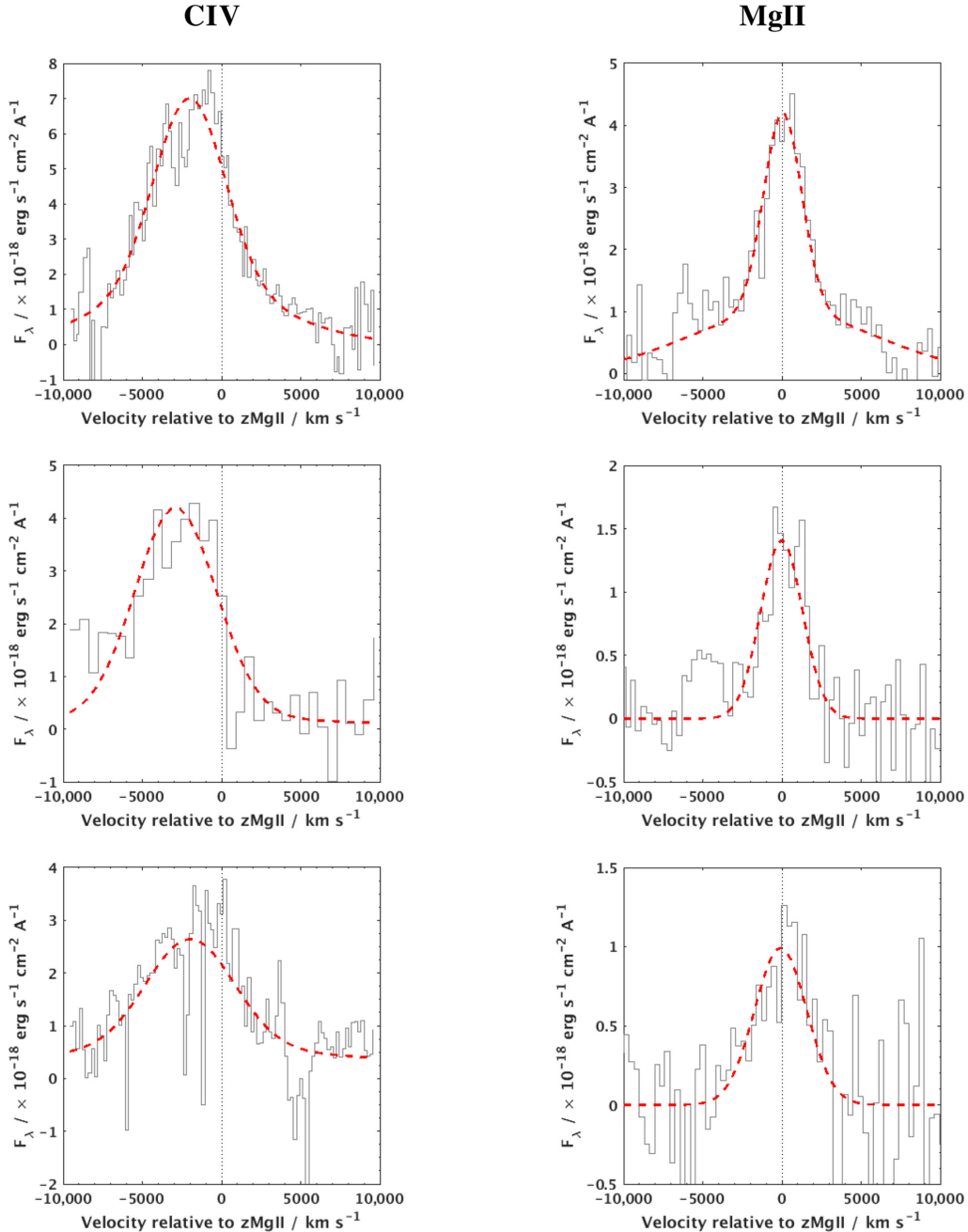


Figure 7. Gaussian fits to the CIV (left) and Mg II (right) emission line profiles for VDES J0224–4711 (top), VDES J0244–5008 (middle), and VDES J0020–3653 (bottom). Zero velocity is defined as the Mg II peak redshift and shown by the dotted vertical lines.

hole masses, Eddington ratios, and CIV blueshifts. The systemic redshifts derived from the Mg II emission lines in these near-infrared spectra are 6.526, 6.724, and 6.834. In two out of the three quasars the Ly α emission line is redshifted by $\delta z \sim 0.01\text{--}0.03$ relative to Mg II. Our new quasars have black hole masses of $\simeq 1\text{--}2 \times 10^9 M_{\odot}$ and are accreting close to or above the Eddington limit, with derived Eddington ratios of $\sim 0.6\text{--}1.1$ in the sample. This is broadly consistent with what is found for other quasars at these highest redshifts (Mazzucchelli et al. 2017; Bañados et al. 2018).

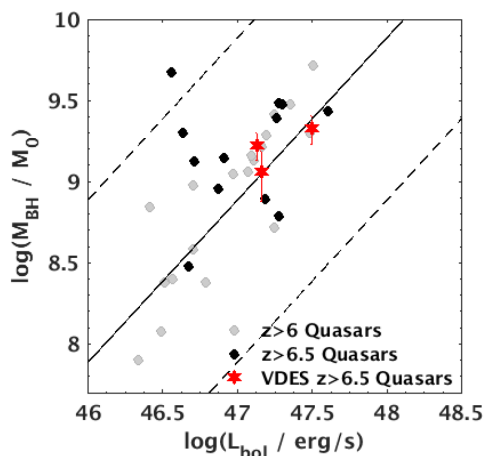
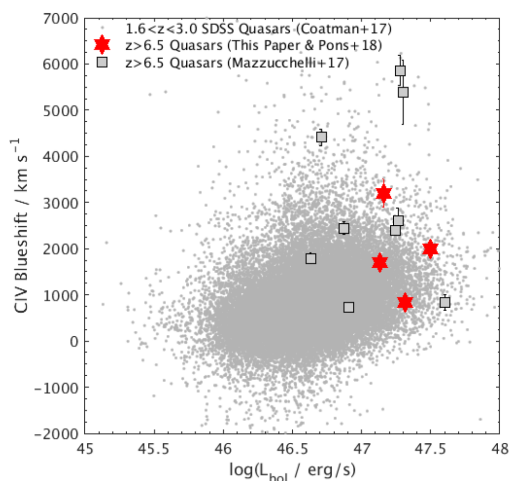
Several of our $z > 6.5$ quasars exhibit large CIV blueshifts of several thousand km s^{-1} . We have demonstrated however that if we compare the sample to lower redshift SDSS quasars of

similar luminosity and where the CIV blueshift is measured in an analogous way to the high-redshift population, the distribution of CIV blueshifts and equivalent widths in our $z > 6.5$ sample is completely consistent with the low-redshift population. Therefore, it appears that high-mass, high-accretion-rate quasars have very similar broad-line region outflow properties regardless of the epoch at which they are observed.

Overall our new quasars now add to the growing census of high-luminosity, highly accreting supermassive black holes seen well into the Epoch of Reionization. Based on extrapolations of the $z \sim 6$ luminosity functions from Willott et al. (2010) and Jiang et al. (2016) we expect to find $\sim 15\text{--}20$ quasars at $6.5 < z < 7.2$ down to a

Table 4. Emission line properties of our three $z > 6.5$ quasars with near-infrared spectroscopy.

	VDES J0020–3653	VDES J0244–5008	VDES J0224–4711
Ly α redshift	6.86 ± 0.01	6.733 ± 0.008	6.514 ± 0.005
Mg II redshift	6.834 ± 0.0004	6.724 ± 0.0008	6.526 ± 0.0003
FWHM _{Mg II} /km s ⁻¹	3800 ± 360	3100 ± 530	3500 ± 310
$\lambda L_{\lambda}(3000)/\text{erg s}^{-1}$	$(2.62 \pm 0.05) \times 10^{46}$	$(2.79 \pm 0.05) \times 10^{46}$	$(6.08 \pm 0.09) \times 10^{46}$
M_{BH}/M_{\odot}	$(1.67 \pm 0.32) \times 10^9$	$(1.15 \pm 0.39) \times 10^9$	$(2.12 \pm 0.42) \times 10^9$
$L_{\text{bol}}/\text{erg s}^{-1}$	$(1.35 \pm 0.03) \times 10^{47}$	$(1.44 \pm 0.02) \times 10^{47}$	$(3.13 \pm 0.04) \times 10^{47}$
$L_{\text{bol}}/L_{\text{Edd}}$	0.62 ± 0.12	0.96 ± 0.33	1.13 ± 0.22
C IV blueshift/km s ⁻¹	1700 ± 100	3200 ± 310	2000 ± 160
C IV EW (rest frame)/Å	55 ± 1	24 ± 2	44 ± 2
M_{1450}	-26.92 ± 0.03	-26.72 ± 0.05	-26.94 ± 0.05


Figure 8. Bolometric luminosity versus black hole mass for the three $z > 6.5$ quasars in this paper (red symbols). These are compared to $z > 6$ and $z > 6.5$ quasars from the literature (De Rosa et al. 2011, 2014; Mazzucchelli et al. 2017). The dashed line denotes an Eddington ratio of 1.

Figure 9. C IV blueshift versus quasar luminosity for the three $z > 6.5$ quasars in this paper and the $z = 6.82$ quasar from Pons et al. (2019; red symbols). These are compared to low-redshift quasars from SDSS as well as the $z > 6.5$ quasars studied in Mazzucchelli et al. (2017).

DES Y -band flux limit of <21.0 and over the full DES survey area of 5000 sq deg. Thus, the four new quasars identified in this paper are expected to form only a small subset of the $z > 6.5$ quasars that will be identified using the final DES + VHS data releases. The number

of $Y < 21.0$ candidates (8; see Section 2.4) found in this work is less than the number of quasars expected from scaling the luminosity function predictions to the area covered by the VHS data. This is likely to be due to the inhomogeneity of the J -band depth of the VHS data, which has a median $J_{5\sigma, \text{AB}}$ depth of 21.4 mag. Thus, we would not expect to recover all quasars with $Y - J < 1.0$ (especially those with very blue colours requiring J -band data deeper than 21.5 mag) to $Y < 21.0$ over the whole area surveyed, leading to a smaller number of candidates compared to that expected for a survey that is 100 per cent complete to $J < 21.0$. The selection function will be fully explored and discussed in a future paper.

ACKNOWLEDGEMENTS

The authors would like to thank Y. Shen for helpful comments and discussions and the referee for valuable insights. SLR, RGM, PCH, and EP acknowledge the support of the UK Science and Technology Facilities Council (STFC). MB acknowledges funding from the STFC via an Ernest Rutherford Fellowship as well as funding from the Royal Society via a University Research Fellowship. Support by European Research Council (ERC) Advanced Grant 320596 ‘The Emergence of Structure during the Epoch of Reionization’ is gratefully acknowledged by RGM. This material is based upon work supported by the National Science Foundation under Grant No. 1615553 to PM.

The analysis presented here is based on observations obtained as part of the VISTA Hemisphere Survey, ESO Programme, 179.A2010 (PI: McMahon). The analysis presented here is based on observations obtained as part of European Southern Observatory (ESO) Programmes 098.A-0439 and 0100.A00346 (PI: McMahon). Based on observations obtained at the Gemini Observatory (Program GS-2016B-FT-8), which is operated by the Association of Universities for Research in Astronomy, Inc., under a cooperative agreement with the NSF on behalf of the Gemini partnership: the National Science Foundation (United States), the National Research Council (Canada), CONICYT (Chile), Ministerio de Ciencia, Tecnología e Innovación Productiva (Argentina), and Ministério da Ciência, Tecnologia e Inovação (Brazil).

Funding for the DES Projects has been provided by the US Department of Energy, the US National Science Foundation, the Ministry of Science and Education of Spain, the Science and Technology Facilities Council of UK, the Higher Education Funding Council for England, the National Center for Supercomputing Applications at the University of Illinois at Urbana-Champaign, the Kavli Institute of Cosmological Physics at the University of Chicago, Financiadora de Estudos e Projetos, Fundação Carlos Chagas Filho de Amparo à Pesquisa do Estado do Rio de Janeiro, Conselho Nacional de

Desenvolvimento Científico e Tecnológico and the Ministério da Ciência e Tecnologia, the Deutsche Forschungsgemeinschaft, and the Collaborating Institutions in the Dark Energy Survey.

The Collaborating Institutions are Argonne National Laboratories, the University of California at Santa Cruz, the University of Cambridge, Centro de Investigaciones Energeticas, Medioambientales y Tecnológicas-Madrid, the University of Chicago, University College London, the DES-Brazil Consortium, the Eidgenössische Technische Hochschule (ETH) Zurich, Fermi National Accelerator Laboratory, the University of Edinburgh, the University of Illinois at Urbana-Champaign, the Institut de Ciències de l'Espai (IEEC/CSIC), the Institut de Física d'Altes Energies, the Lawrence Berkeley National Laboratory, the Ludwig-Maximilians Universität and the associated Excellence Cluster Universe, the University of Michigan, the National Optical Astronomy Observatory, the University of Nottingham, The Ohio State University, the University of Pennsylvania, the University of Portsmouth, SLAC National Laboratory, Stanford University, the University of Sussex, and Texas A&M University.

This analysis makes use of the `cosmics.py` algorithm based on the L.A. Cosmic algorithm detailed in van Dokkum (2001).

REFERENCES

- Abbott T. M. C. et al., 2018, *ApJS*, 239, 18
 Bañados E. et al., 2016, *ApJS*, 227, 11
 Bañados E. et al., 2018, *Nature*, 553, 473
 Banerji M. et al., 2015, *MNRAS*, 446, 2523
 Baskin A., Laor A., 2005, *MNRAS*, 356, 1029
 Becker G. D., Sargent W. L. W., Rauch M., Carswell R. F., 2012, *ApJ*, 744, 91
 Bolton J. S., Haehnelt M. G., 2007, *MNRAS*, 374, 493
 Coatman L., Hewett P. C., Banerji M., Richards G. T., 2016, *MNRAS*, 461, 647
 Coatman L., Hewett P. C., Banerji M., Richards G. T., Hennawi J. F., Prochaska J. X., 2017, *MNRAS*, 465, 2120
 De Rosa G., Decarli R., Walter F., Fan X., Jiang L., Kurk J., Pasquali A., Rix H. W., 2011, *ApJ*, 739, 56
 De Rosa G. et al., 2014, *ApJ*, 790, 145
 Eilers A.-C., Davies F. B., Hennawi J. F., Prochaska J. X., Lukić Z., Mazzucchelli C., 2017, *ApJ*, 840, 24
 Fan X., Carilli C. L., Keating B., 2006, *ARA&A*, 44, 415
 Hewett P. C., Wild V., 2010, *MNRAS*, 405, 2302
 Horne K., 1986, *PASP*, 98, 609
 Jiang L. et al., 2016, *ApJ*, 833, 222
 Jones A., Noll S., Kausch W., Szyszka C., Kimeswenger S., 2013, *A&A*, 560, A91
 Kelson D. D., 2003, *PASP*, 115, 688
 Kirkpatrick J. D., Cushing M. C., Gelino C. R., Griffith R. L., Skyrutskie M. F., Marsh K. A., Wright E. L., Mainzer A., 2011, *ApJS*, 197, 19
 Konigl A., Kartje J. F., 1994, *ApJ*, 434, 446
 Latif M. A., Schleicher D. R. G., Schmidt W., Niemeyer J., 2013, *MNRAS*, 433, 1607
 López S. et al., 2016, *A&A*, 594, A91
 Maddox N., Hewett P. C., 2006, *MNRAS*, 367, 717
 Maddox N., Hewett P. C., Péroux C., Nestor D. B., Williamsstotzki L., 2012, *MNRAS*, 424, 2876
 Matsuoka Y. et al., 2018a, *PASJ*, 70, S35
 Matsuoka Y. et al., 2018b, *ApJS*, 237, 5
 Mazzucchelli C. et al., 2017, *ApJ*, 849, 91
 McMahon R. G., Banerji M., Gonzalez E., Kogosov S. E., Bejar B. V. J., Lodiou N., Rebolo R., VHS Collaboration, 2013, *The Messenger*, 154, 35
 Meisner A. M., Lang D., Schlegel D. J., 2017, *AJ*, 154, 161
 Mortlock D. J. et al., 2011, *Nature*, 474, 616
 Murray N., Chiang J., Grossman S. A., Voit G. M., 1995, *ApJ*, 451, 498
 Noll S., Kausch W., Barden M., Jones A. M., Szyszka C., Kimeswenger S., Vinther J., 2012, *A&A*, 543, A92
 Pons E., McMahon R. G., Simcoe R. A., Banerji M., Hewett P. C., Reed S. L., 2019, *MNRAS*, 484, 5142
 Reed S. L. et al., 2017, *MNRAS*, 468, 4702 (R17)
 Richards G. T. et al., 2011, *AJ*, 141, 167
 Richards G. T., Fan X., Newberg H. J., Strauss M. A., Vanden Berk D. E., Schneider D. P., Yanny B., 2002, *AJ*, 123, 2945
 Shen Y. et al., 2011, *ApJS*, 194, 45
 Shen Y. et al., 2016, *ApJ*, 831, 7
 Shen Y. et al., 2019, *ApJ*, 873, 35
 Sijacki D., Springel V., Haehnelt M. G., 2009, *MNRAS*, 400, 100
 Skrzypczak N., Warren S. J., Faherty J. K., Modesrtlock D. J., Burgasser A. J., Hewett P. C., 2015, *A&A*, 574, A78
 van Dokkum P. G., 2001, *PASP*, 113, 1420
 Venemans B. P. et al., 2013, *ApJ*, 779, 24
 Venemans B. P. et al., 2015a, *MNRAS*, 453, 2259
 Venemans B. P. et al., 2015b, *ApJ*, 801, L11
 Venemans B. P., Walter F., Zschaechner L., Decarli R., De Rosa G., Findlay J. R., McMahon R. G., Sutherland W. J., 2016, *ApJ*, 816, 37
 Vestergaard M., Osmer P. S., 2009, *ApJ*, 699, 800
 Vestergaard M., Wilkes B. J., 2001, *ApJS*, 134, 1
 Volonteri M., 2010, *A&AR*, 18, 279
 Wang F. et al., 2017, *ApJ*, 839, 27
 Wang F. et al., 2018, preprint ([arXiv:1810.11926](https://arxiv.org/abs/1810.11926))
 Willott C. J. et al., 2010, *AJ*, 139, 906
 Wright E. L. et al., 2010, *ApJ*, 140, 1868
 Yang J. et al., 2018, preprint ([arXiv:1811.11915](https://arxiv.org/abs/1811.11915))
- ¹*Department of Astrophysical Sciences, Princeton University, 4 Ivy Lane, Princeton, NJ 08544, USA*
²*Institute of Astronomy, University of Cambridge, Madingley Road, Cambridge CB3 0HA, UK*
³*Kavli Institute for Cosmology, University of Cambridge, Madingley Road, Cambridge CB3 0HA, UK*
⁴*Department of Physics and Astronomy, University of California, 900 University Avenue, Riverside, CA 92521, USA*
⁵*Center for Cosmology and Astro-Particle Physics, The Ohio State University, Columbus, OH 43210, USA*
⁶*Department of Astronomy, The Ohio State University, Columbus, OH 43210, USA*
⁷*Observatories of the Carnegie Institution for Science, 813 Santa Barbara Street, Pasadena, CA 91101, USA*
⁸*Cerro Tololo Inter-American Observatory, National Optical Astronomy Observatory, Casilla 603, La Serena, Chile*
⁹*Fermi National Accelerator Laboratory, PO Box 500, Batavia, IL 60510, USA*
¹⁰*Institute of Cosmology and Gravitation, University of Portsmouth, Portsmouth PO1 3FX, UK*
¹¹*CNRS, UMR 7095, Institut d'Astrophysique de Paris, F-75014 Paris, France*
¹²*Sorbonne Universités, UPMC Univ Paris 06, UMR 7095, Institut d'Astrophysique de Paris, F-75014 Paris, France*
¹³*Department of Physics & Astronomy, University College London, Gower Street, London WC1E 6BT, UK*
¹⁴*Centro de Investigaciones Energéticas, Medioambientales y Tecnológicas (CIEMAT), E-28040 Madrid, Spain*
¹⁵*Laboratório Interinstitucional de e-Astronomia - LIneA, Rua Gal. José Cristino 77, Rio de Janeiro, RJ-20921-400, Brazil*
¹⁶*Department of Astronomy, University of Illinois at Urbana-Champaign, 1002 W. Green Street, Urbana, IL 61801, USA*
¹⁷*National Center for Supercomputing Applications, 1205 West Clark St., Urbana, IL 61801, USA*
¹⁸*Institiut de Física d'Altes Energies (IFAE), The Barcelona Institute of Science and Technology, Campus UAB, E-08193 Bellaterra (Barcelona), Spain*

¹⁹*Institut d'Estudis Espacials de Catalunya (IEEC), E-08034 Barcelona, Spain*

²⁰*Institute of Space Sciences (ICE, CSIC), Campus UAB, Carrer de Can Magrans, s/n, E-08193 Barcelona, Spain*

²¹*Kavli Institute for Particle Astrophysics & Cosmology, P. O. Box 2450, Stanford University, Stanford, CA 94305, USA*

²²*Department of Physics and Astronomy, University of Pennsylvania, Philadelphia, PA 19104, USA*

²³*Observatório Nacional, Rua Gal. José Cristino 77, Rio de Janeiro, RJ - 20921-400, Brazil*

²⁴*Department of Physics, IIT Hyderabad, Kandi, Telangana 502285, India*

²⁵*Department of Astronomy, University of Michigan, Ann Arbor, MI 48109, USA*

²⁶*Department of Physics, University of Michigan, Ann Arbor, MI 48109, USA*

²⁷*Kavli Institute for Cosmological Physics, University of Chicago, Chicago, IL 60637, USA*

²⁸*Instituto de Física Teórica UAM/CSIC, Universidad Autónoma de Madrid, E-28049 Madrid, Spain*

²⁹*Department of Physics, Stanford University, 382 Via Pueblo Mall, Stanford, CA 94305, USA*

³⁰*SLAC National Accelerator Laboratory, Menlo Park, CA 94025, USA*

³¹*Santa Cruz Institute for Particle Physics, Santa Cruz, CA 95064, USA*

³²*Department of Physics, The Ohio State University, Columbus, OH 43210, USA*

³³*Max Planck Institute for Extraterrestrial Physics, Giessenbachstrasse, D-85748 Garching, Germany*

³⁴*Universitäts-Sternwarte, Fakultät für Physik, Ludwig-Maximilians Universität München, Scheinerstr. 1, D-81679 München, Germany*

³⁵*Harvard-Smithsonian Center for Astrophysics, Cambridge, MA 02138, USA*

³⁶*Australian Astronomical Optics, Macquarie University, North Ryde, NSW 2113, Australia*

³⁷*Departamento de Física Matemática, Instituto de Física, Universidade de São Paulo, CP 66318, São Paulo, SP 05314-970, Brazil*

³⁸*George P. and Cynthia Woods Mitchell Institute for Fundamental Physics and Astronomy, and Department of Physics and Astronomy, Texas A&M University, College Station, TX 77843, USA*

³⁹*Institució Catalana de Recerca i Estudis Avançats, E-08010 Barcelona, Spain*

⁴⁰*Jet Propulsion Laboratory, California Institute of Technology, 4800 Oak Grove Dr., Pasadena, CA 91109, USA*

⁴¹*School of Physics and Astronomy, University of Southampton, Southampton SO17 1BJ, UK*

⁴²*Instituto de Física Gleb Wataghin, Universidade Estadual de Campinas, Campinas, SP13083-859, Brazil*

⁴³*Computer Science and Mathematics Division, Oak Ridge National Laboratory, Oak Ridge, TN 37831, USA*

⁴⁴*Argonne National Laboratory, 9700 South Cass Avenue, Lemont, IL 60439, USA*

This paper has been typeset from a $\text{\TeX}/\text{\LaTeX}$ file prepared by the author.